PHYSICAL REVIEW B **91**, 235305 (2015)

Quantitative description of photoexcited scanning tunneling spectroscopy and its application to the GaAs(110) surface

M. Schnedler, V. Portz, P. H. Weidlich, R. E. Dunin-Borkowski, and Ph. Ebert[*]
Peter Grünberg Institut, Forschungszentrum Jülich GmbH, 52425 Jülich, Germany

(Received 19 November 2014; revised manuscript received 19 May 2015; published 4 June 2015)

A quantitative description of photoexcited scanning tunneling spectra is developed and applied to photoexcited spectra measured on p-doped nonpolar GaAs(110) surfaces. Under illumination, the experimental spectra exhibit an increase of the tunnel current at negative sample voltages only. In order to analyze the experimental data quantitatively, the potential and charge-carrier distributions of the photoexcited tip-vacuum-semiconductor system are calculated by solving the Poisson as well as the hole and electron continuity equations by a finite-difference algorithm. On this basis, the different contributions to the tunnel current are calculated using an extension of the model of Feenstra and Stroscio to include the light-excited carrier concentrations. The best fit of the calculated tunnel currents to the experimental data is obtained for a tip-induced band bending, which is limited by the partial occupation of the C_3 surface state by light-excited electrons. The tunnel current at negative voltages is then composed of a valence band contribution and a photoinduced tunnel current of excited electrons in the conduction band. The quantitative description of the tunnel current developed here is generally applicable and provides a solid foundation for the quantitative interpretation of photoexcited scanning tunneling spectroscopy.

DOI: 10.1103/PhysRevB.91.235305 PACS number(s): 61.80.Ba, 68.37.Ef, 68.47.Fg

I. INTRODUCTION

The efficiency of solar cell and optoelectronic devices is closely connected to the nanoscale distribution of charge carriers. For example, defects can give rise to nonradiative carrier recombination centers, reducing the charge-carrier concentration locally [1,2]. Such effects are detrimental to both the electron-light and light-electron conversion efficiencies in optoelectronic and solar cell devices, respectively. In order to understand the physical processes involved at the atomic scale, the materials used in the device structures need to be investigated simultaneously under illumination and with atomic resolution.

Photoexcited scanning tunneling spectroscopy (STS) [3] is ideally suited to probe the illumination-induced local surface photovoltage, band bending, carrier concentration, and the electrostatic potential distribution with atomic resolution [1,2,4–10]. For a quantitative analysis, particularly of the local charge-carrier concentration and redistribution, a fundamental physical understanding and theoretical modeling of the photoexcited tunneling spectra would be needed. Grafström pointed out that a realistic model "should allow the various quantities involved, such as recombination rates and tip-induced band bending, to be identified more reliably and should put the interpretation of spatial variations of the measurement signal on a more solid ground"[11]. However, to date, mostly qualitative explanations attribute the photoexcited tunneling spectra to changes of the band bending under illumination [4,7,8,12–17]. Reliable quantitative simulations of and fits to photoexcited tunneling spectra are still lacking.

Prins *et al.* [18], Sommerhalter *et al.* [19], and Vu *et al.* [20] developed first approaches to the problem. Prins *et al.* focused on pinned surfaces with a high density of surface gap states, but did not take into account tunneling into the conduction and out of the valence band. Sommerhalter *et al.* modeled unpinned surfaces without surface gap states using a one-dimensional metal-insulator-semiconductor model. Both approximated the tunneling current with a thermionic emission current model, which according to Sommerhalter *et al.* represents a simplification compared to the earlier method presented by Feenstra and Stroscio [21]. In addition the one-dimensional model used by Sommerhalter *et al.* as well as the planar one-dimensional GaAs-insulator-Au tunnel contact measured and simulated by Vu *et al.* do not take into account the localized nature of the STM tip, which significantly affects the electric field distribution near the tip apex and thus band bending [22].

In this paper we present a generally applicable and detailed three-dimensional quantitative description of the effect of illumination on the tunneling current. We use a three-dimensional finite-difference calculation of the electrostatic potential in a tip-vacuum-semiconductor sample system, by solving the Poisson equation and the continuity equations for holes and electrons. On the basis of the obtained electrostatic potential, the different contributions to the tunneling current are calculated using the tunneling model of Feenstra *et al.* [21] but extended for tunneling of light-generated carriers. The calculated tunnel current is compared quantitatively to laser-excited tunneling spectra measured from GaAs(110) surfaces. A detailed discussion of the different tunnel current contributions with and without laser excitation is provided. This analysis demonstrates that the modeling developed here provides a comprehensive quantitative description of photoexcited tunneling spectra.

II. EXPERIMENT

For the laser-excited STS experiments we used nonpolar GaAs(110) surfaces as model system. GaAs was chosen for simplicity, but any other semiconductor that exhibits a band gap smaller than the photon energy of the laser can be used, too. Samples cut from a p-doped GaAs(001) wafer

---

[*] p.ebert@fz-juelich.de

([Zn] = (1-2) × 10^{18} cm^{-3}) were freshly cleaved *in situ*, at a pressure of 1 × 10^{-10} mbar, to obtain clean (110) surfaces. The cleavage surfaces used for the experiments consisted of very large atomically flat terraces separated by steps. Only a very low, typical [23–25], defect concentration of $\lesssim 5 \times 10^{10}$ cm^{-2} was present. Thus *no* relevant concentrations of *extrinsic* surface states and hence no *extrinsic* pinning can be expected [26].

The sample was illuminated with a (0.95 ± 0.05) mW diode laser through a window flange at an angle of incidence of (62 ± 3)°. We used a wavelength of 785 nm (corresponding to an energy of 1.58 eV, which is larger than the band gap). With the help of two micrometer screws, the beam direction could be adjusted precisely in order to hit the sample exactly at the tip position. The focusing of the beam spot was achieved by a built-in lens directly in front of the laser. We measured the spot size in units of the width of the sample, which was determined previously with a calibrated optical microscope. The smallest focus, which we achieved was elliptical (due to the inclined incident angle) with major and minor axes of (50 ± 10) and (100 ± 20) μm and a roughly constant irradiance profile. The irradiance of the laser beam was furthermore weakened by the transmission through the lens, the window flange and the reflection on the sample. We calculated the reflection at the GaAs surface for an incident angle of (62 ± 3)° to (30.5 ± 0.5)% and the losses at the window flange and lenses to (7 ± 1)%. Hence, (60.1 ± 1)% of the original irradiance is deposited in the GaAs sample. This corresponds to an average irradiance of (1.45 ± 0.44) × 10^5 Wm^{-2}. Note, the laser irradiance and tip-sample separations (i.e., tunneling set points) chosen represent a compromise between the magnitude of the photo-induced tunnel current, the limitations by the preamplifier dynamics, and the stability of the tunnel system (i.e., to avoid changing or destroying the surface and tip apex).

Unlike many other experiments, we decided not to use a mechanical chopper, since the laser intensity may be influenced by a partially concealed laser beam (laser intensity changes gradually at the chopper edges). Hence, during the acquisition of current-voltage spectra, the laser was electrically modulated by the STS control electronics. In contrast to standard current-voltage spectra, we consecutively measured the current with and without illumination at each voltage step. Each of these steps took 1280 μs, during which first the laser was turned on for 180 μs only to minimize thermal drift. Second, the current without illumination was then acquired 800 μs after turning off the laser. Importantly, the current-voltage spectra with and without illumination were hence probed at the same tip-sample separation, which was fixed by the set voltage and current without illumination.

We used electrochemically etched tungsten tips in our STM measurements. The most relevant parameter for a quantitative analysis is the radius of curvature of the tip apex. Using TEM images we determined a radius of curvature of 10 nm for tungsten tips etched by our setup [27]. This value is also used in the calculation. Furthermore, tungsten tips were chosen, since this material is known to exhibit negligible tip-enhanced raman spectroscopy effects, since the plasmon resonance is in deep IR, outside the range of the laser wavelength used in the experiment [28,29].

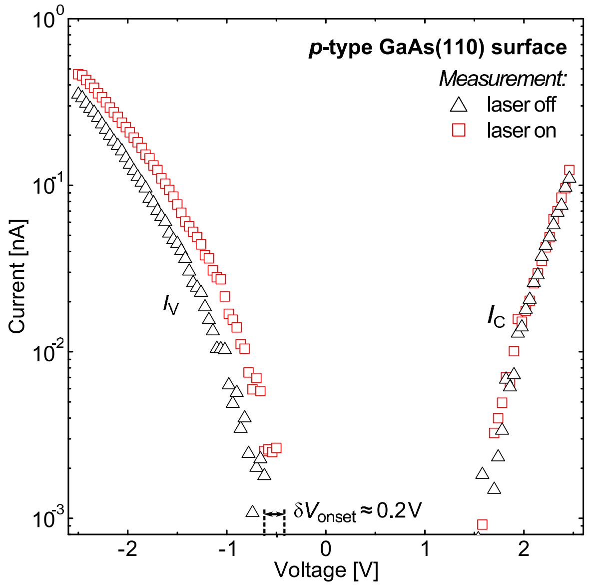

FIG. 1. (Color online) Current-voltage spectra obtained on a p-doped GaAs(110) surface with (red squares) and without (black triangles) illumination for identical tip-sample separations. The set point is −2.0 V and 150 pA (without illumination). Without laser excitation the current at positive (negative) voltages arises from electrons tunneling into the conduction band labeled I_C (out of the valence band, I_V) [30]. The laser excitation increases the tunnel current only at negative sample voltages. At positive voltages no effect is detectable.

III. EXPERIMENTAL RESULTS

Figure 1 shows two current-voltage spectra obtained simultaneously at identical tip-sample separations using the previously described method. The spectrum shown with (black) triangles has been measured in dark. The (red) squares represent the spectrum measured under illumination. At positive voltages both spectra coincide and have identical onset voltages of about +1.7 V. However, at negative voltages, the current measured under illumination is higher than that measured without light. In addition, the illumination shifts the onset voltage of the spectrum from −0.6 V (dark) to −0.4 V (illuminated).

The two spectra shown are representative of a larger set of measurements done on several GaAs(110) surfaces. The common features of these measurements are: (i) no change of the tunnel current at positive voltages by illumination, (ii) illumination increases the tunnel current at negative voltages, and (iii) the onset voltage of the tunnel current at negative voltages is always close to −0.4 V under illumination using a laser energy of 1.58 eV (785 nm). Note, under dark conditions the onset voltage for tunneling at negative voltages naturally shifts downward for lower doped samples due to the increasing band bending [31] We demonstrate the feasibility of this type of analysis using the chosen spectra.

IV. THEORETICAL MODEL

In order to interpret laser-excited tunneling spectroscopy, such as the example shown in Fig. 1, we recall that due to the negligible concentration of surface states within the fundamental band gap and the moderate doping concentration of $2 \times 10^{18}\,\mathrm{cm}^{-3}$, the applied electric field between the tip and the sample is not fully screened at the surface and penetrates into the semiconductor. This induces a so-called tip-induced band bending [21,32,33], which is qualitatively reduced with increasing free charge-carrier concentration [30,31,34]. Hence, the onset voltages contain information about the distribution of charge carriers [35,36].

Figure 1 shows that the onset voltage of the conduction band current I_C (at positive sample voltages) remains unchanged under illumination. This is due to the upward band bending, screened with and without illumination by the accumulation of majority carriers at the surface. Therefore, the upward band bending is not altered significantly and the tunnel current remains essentially unchanged. In contrast, the onset voltage of the valence band current I_V (negative sample voltages) is shifted toward smaller negative voltages by $\delta V_\mathrm{onset} \approx +0.2$ V under illumination (Fig. 1). This indicates the presence of light-excited minority carriers at the semiconductor's surface, whose concentration is orders of magnitude higher than that of thermally generated *minority* carriers. These minority carriers, on the one hand, can directly tunnel into the tip. On the other hand, they may enhance the screening, reducing the downward band bending at negative voltages under illumination and hence increasing the valence band tunnel current. The relative magnitude of these two effects is unclear and needs to be investigated quantitatively. Therefore, a derivation of the electrostatic potential, the electron concentration, and the hole concentration as well as the calculation of the tunnel current under illumination will be developed and illustrated in the following.

A. Electrostatic potential and carrier distribution

As outlined above, the calculation of the tunnel current requires the electrostatic potential distribution for a biased metal tip-vacuum-semiconductor system. This system requires a full three-dimensional solution of the Poisson equation, since a one-dimensional analytical solution, as, e.g., given by Seiwatz and Green [37] does not consider the effect of the localized shape of the tip on the electrostatic potential. In this section we describe the approach used for calculating the electrostatic potential and charge-carrier distributions. For the sake of completeness, we first recall those fundamental semiconductor equations that are needed for further derivations in this work, followed by the evaluation of equations suitable for numerical iterations.

1. System of differential equations

Thus far, Feenstra solved this kind of electrostatic problem using a finite-difference method to iteratively solve the Poisson equation [22]. The charge densities in the semiconductor are assumed to follow the effective mass approximations. For the conduction band, this approximation is given by [38]

$$n_0 = N_\mathrm{C} \frac{2}{\sqrt{\pi}} F_{1/2}\left(\frac{E_\mathrm{F} - E_\mathrm{C}}{kT}\right), \tag{1}$$

where k is the Boltzmann constant, E_F is the Fermi level, E_C is the minimum of the conduction band, and $F_{1/2}$ is the Fermi-Dirac integral. N_C is the effective density of states of the conduction band, given by $N_\mathrm{C} = 2(2\pi m_{\mathrm{eff,C}} kT/h^2)^{3/2}$, where h is the Planck constant and $m_{\mathrm{eff,C}}$ is the density of states effective mass for electrons. For the charge density of the valence band, the approximation is given by

$$p_0 = N_\mathrm{V} \frac{2}{\sqrt{\pi}} F_{1/2}\left(\frac{E_\mathrm{V} - E_\mathrm{F}}{kT}\right), \tag{2}$$

where E_V is the maximum of the valence band. N_V is the effective density of states of the valence band given by $N_\mathrm{V} = 2(2\pi m_{\mathrm{eff,V}} kT/h^2)^{3/2}$. $m_{\mathrm{eff,V}}$ is the effective density of states mass for holes. Besides some material properties and the temperature, which is assumed to be constant, the electron and hole densities in the effective mass approximation depend only on the position of the valence and conduction band edges relative to the Fermi energy. Hence, these equations do not hold for the description of additional excess carriers generated by photon interaction.

Thus, here we additionally introduce the continuity equations for electrons and holes. This will give a more general description of the problem, enabling the introduction of carrier generation and recombination. Overall, it is necessary to solve three coupled partial differential equations:

The Poisson equation for the electrostatic potential $\phi(x,y,z)$ at the position (x,y,z) is given by

$$\Delta\phi(x,y,z) + \frac{e}{\epsilon_0\epsilon_\mathrm{r}}[p(x,y,z) - n(x,y,z) + N_\mathrm{D}^+ - N_\mathrm{A}^-] = 0, \tag{3}$$

where e is the (unsigned) electron charge, ϵ_0 is the vacuum permittivity, ϵ_r is the relative permittivity of the semiconductor, and $n(x,y,z)$ and $p(x,y,z)$ are the electron and hole concentrations at position (x,y,z), respectively. The density of ionized donors N_D^+ and acceptors N_A^- are defined as [37]

$$N_\mathrm{D}^+ = N_\mathrm{D}\{1 + 2\exp[(E_\mathrm{F} - E_\mathrm{D})/kT]\}^{-1}, \tag{4}$$

$$N_\mathrm{A}^- = N_\mathrm{A}\{1 + 2\exp[(E_\mathrm{A} - E_\mathrm{F})/kT]\}^{-1}, \tag{5}$$

respectively, where N_D (N_A) is the concentration of donors (acceptors) and E_D (E_A) the respective energy level. Note that E_D and E_A as well as E_V and E_C are shifted by $e\phi(x,y,z)$ in the region of nonzero band bending.

Assuming a time-invariant charge distribution, the continuity equations for electrons and holes are

$$\nabla \cdot \vec{J}_\mathrm{n} - eR = 0, \tag{6}$$

$$\nabla \cdot \vec{J}_\mathrm{p} + eR = 0, \tag{7}$$

where R is a time-averaged generation or recombination rate and $\vec{J}_\mathrm{n}$ ($\vec{J}_\mathrm{p}$) is the current density for electrons (holes). $\vec{J}_\mathrm{n}$ and $\vec{J}_\mathrm{p}$ can be separated into drift and diffusion terms [39]:

$$\vec{J}_\mathrm{n} = e[\mu_\mathrm{n} n(x,y,z)\vec{E} + D_\mathrm{n}\nabla n(x,y,z)], \tag{8}$$

$$\vec{J}_\mathrm{p} = e[\mu_\mathrm{p} p(x,y,z)\vec{E} - D_\mathrm{p}\nabla p(x,y,z)], \tag{9}$$

where μ_n (μ_p) is the mobility and D_n (D_p) is the diffusion coefficient of electrons (holes) in the semiconductor. D_n (D_p) is connected to μ_n (μ_p) by the Einstein relation. Note, we assume the mobility (and the diffusion coefficient) to be location-independent in this calculation. Inserting Eqs. (8) and (9) into Eqs. (6) and (7), respectively, and using the relation $\vec{E} = -\nabla\phi$, the continuity equations become

$$\nabla \cdot [D_\mathrm{n}\nabla n(x,y,z) - \mu_\mathrm{n} n(x,y,z)\nabla\phi] - R = 0, \tag{10}$$

$$\nabla \cdot [D_\mathrm{p}\nabla p(x,y,z) + \mu_\mathrm{p} p(x,y,z)\nabla\phi] - R = 0. \tag{11}$$

2. *Difference equations*

Equations (3), (10), and (11) represent a system of three coupled partial differential equations that cannot be solved analytically in full generality [39]. For numerical computations we need adequate *difference* equations for these *differential* equations. We decided to follow Selberherr's discretization approach of directly replacing the differential operators by the corresponding difference operators.

The derivation of the discretized Poisson equation replacing Eq. (3) is straightforward, since the Laplace operator has to be replaced, only. It is given by [39]

$$\begin{aligned}&\left(\frac{\frac{\phi_\mathrm{i+1,j,k}-\phi_\mathrm{i,j,k}}{x_\mathrm{i+1}-x_\mathrm{i}} - \frac{\phi_\mathrm{i,j,k}-\phi_\mathrm{i-1,j,k}}{x_\mathrm{i}-x_\mathrm{i-1}}}{\frac{x_\mathrm{i+1}-x_\mathrm{i-1}}{2}} + \frac{\frac{\phi_\mathrm{i,j+1,k}-\phi_\mathrm{i,j,k}}{y_\mathrm{j+1}-y_\mathrm{j}} - \frac{\phi_\mathrm{i,j,k}-\phi_\mathrm{i,j-1,k}}{y_\mathrm{j}-y_\mathrm{j-1}}}{\frac{y_\mathrm{j+1}-y_\mathrm{j-1}}{2}}\right.\\ &\quad\left.+\frac{\frac{\phi_\mathrm{i,j,k+1}-\phi_\mathrm{i,j,k}}{z_\mathrm{k+1}-z_\mathrm{k}} - \frac{\phi_\mathrm{i,j,k}-\phi_\mathrm{i,j,k-1}}{z_\mathrm{k}-z_\mathrm{k-1}}}{\frac{z_\mathrm{k+1}-z_\mathrm{k-1}}{2}}\right)\\ &\quad+\frac{e}{\epsilon_0\epsilon_\mathrm{r}}\left(-n_\mathrm{i,j,k}+p_\mathrm{i,j,k}+N_\mathrm{D}^{+}-N_\mathrm{A}^{-}\right)=0.\end{aligned} \tag{12}$$

Note, since the finite-difference method uses a mesh of discrete points (which are in general not equidistant), the continuous physical coordinates (x,y,z) become discrete indices (i,j,k), which are mapped to discrete physical coordinates $(x_\mathrm{i},y_\mathrm{j},z_\mathrm{k})$. Hence, e.g., $\phi_\mathrm{i,j,k}$ is an abbreviated notation for $\phi(x_\mathrm{i},y_\mathrm{j},z_\mathrm{k})$.

The derivation of the discretized continuity equations for holes and electrons is more complex and is derived in analogy to Ref. [39] (starting on page 155) for the three-dimensional case here. The resulting discretized continuity equation for electrons is

$$\begin{aligned}&\frac{B\left(\frac{\phi_\mathrm{i+1,j,k}-\phi_\mathrm{i,j,k}}{kT}\right)n_\mathrm{i+1,j,k} - B\left(\frac{\phi_\mathrm{i,j,k}-\phi_\mathrm{i+1,j,k}}{kT}\right)n_\mathrm{i,j,k}}{(x_\mathrm{i+1}-x_\mathrm{i})\frac{x_\mathrm{i+1}-x_\mathrm{i-1}}{2}}\\ &-\frac{B\left(\frac{\phi_\mathrm{i,j,k}-\phi_\mathrm{i-1,j,k}}{kT}\right)n_\mathrm{i,j,k} - B\left(\frac{\phi_\mathrm{i-1,j,k}-\phi_\mathrm{i,j,k}}{kT}\right)n_\mathrm{i-1,j,k}}{(x_\mathrm{i}-x_\mathrm{i-1})\frac{x_\mathrm{i+1}-x_\mathrm{i-1}}{2}}\\ &+\frac{B\left(\frac{\phi_\mathrm{i,j+1,k}-\phi_\mathrm{i,j,k}}{kT}\right)n_\mathrm{i,j+1,k} - B\left(\frac{\phi_\mathrm{i,j,k}-\phi_\mathrm{i,j+1,k}}{kT}\right)n_\mathrm{i,j,k}}{(y_\mathrm{j+1}-y_\mathrm{j})\frac{y_\mathrm{j+1}-y_\mathrm{j-1}}{2}}\\ &-\frac{B\left(\frac{\phi_\mathrm{i,j,k}-\phi_\mathrm{i,j-1,k}}{kT}\right)n_\mathrm{i,j,k} - B\left(\frac{\phi_\mathrm{i,j-1,k}-\phi_\mathrm{i,j,k}}{kT}\right)n_\mathrm{i,j-1,k}}{(y_\mathrm{j}-y_\mathrm{j-1})\frac{y_\mathrm{j+1}-y_\mathrm{j-1}}{2}}\\ &+\frac{B\left(\frac{\phi_\mathrm{i,j,k+1}-\phi_\mathrm{i,j,k}}{kT}\right)n_\mathrm{i,j,k+1} - B\left(\frac{\phi_\mathrm{i,j,k}-\phi_\mathrm{i,j,k+1}}{kT}\right)n_\mathrm{i,j,k}}{(z_\mathrm{k+1}-z_\mathrm{k})\frac{z_\mathrm{k+1}-z_\mathrm{k-1}}{2}}\\ &-\frac{B\left(\frac{\phi_\mathrm{i,j,k}-\phi_\mathrm{i,j,k-1}}{kT}\right)n_\mathrm{i,j,k} - B\left(\frac{\phi_\mathrm{i,j,k-1}-\phi_\mathrm{i,j,k}}{kT}\right)n_\mathrm{i,j,k-1}}{(z_\mathrm{k}-z_\mathrm{k-1})\frac{z_\mathrm{k+1}-z_\mathrm{k-1}}{2}} - \frac{R}{D_\mathrm{n}} = 0,\end{aligned} \tag{13}$$

with the Bernoulli function $B(x) = x/[\exp(x) - 1]$. Analogously, the discretized continuity equation for holes can be found to be [39]

$$\begin{aligned}&\frac{B\left(\frac{\phi_\mathrm{i,j,k}-\phi_\mathrm{i+1,j,k}}{kT}\right)p_\mathrm{i+1,j,k} - B\left(\frac{\phi_\mathrm{i+1,j,k}-\phi_\mathrm{i,j,k}}{kT}\right)p_\mathrm{i,j,k}}{(x_\mathrm{i+1}-x_\mathrm{i})\frac{x_\mathrm{i+1}-x_\mathrm{i-1}}{2}}\\ &-\frac{B\left(\frac{\phi_\mathrm{i-1,j,k}-\phi_\mathrm{i,j,k}}{kT}\right)p_\mathrm{i,j,k} - B\left(\frac{\phi_\mathrm{i,j,k}-\phi_\mathrm{i-1,j,k}}{kT}\right)p_\mathrm{i-1,j,k}}{(x_\mathrm{i}-x_\mathrm{i-1})\frac{x_\mathrm{i+1}-x_\mathrm{i-1}}{2}}\\ &+\frac{B\left(\frac{\phi_\mathrm{i,j,k}-\phi_\mathrm{i,j+1,k}}{kT}\right)p_\mathrm{i,j+1,k} - B\left(\frac{\phi_\mathrm{i,j+1,k}-\phi_\mathrm{i,j,k}}{kT}\right)p_\mathrm{i,j,k}}{(y_\mathrm{j+1}-y_\mathrm{j})\frac{y_\mathrm{j+1}-y_\mathrm{j-1}}{2}}\\ &-\frac{B\left(\frac{\phi_\mathrm{i,j-1,k}-\phi_\mathrm{i,j,k}}{kT}\right)p_\mathrm{i,j,k} - B\left(\frac{\phi_\mathrm{i,j,k}-\phi_\mathrm{i,j-1,k}}{kT}\right)p_\mathrm{i,j-1,k}}{(y_\mathrm{j}-y_\mathrm{j-1})\frac{y_\mathrm{j+1}-y_\mathrm{j-1}}{2}}\\ &+\frac{B\left(\frac{\phi_\mathrm{i,j,k}-\phi_\mathrm{i,j,k+1}}{kT}\right)p_\mathrm{i,j,k+1} - B\left(\frac{\phi_\mathrm{i,j,k+1}-\phi_\mathrm{i,j,k}}{kT}\right)p_\mathrm{i,j,k}}{(z_\mathrm{k+1}-z_\mathrm{k})\frac{z_\mathrm{k+1}-z_\mathrm{k-1}}{2}}\\ &-\frac{B\left(\frac{\phi_\mathrm{i,j,k-1}-\phi_\mathrm{i,j,k}}{kT}\right)p_\mathrm{i,j,k} - B\left(\frac{\phi_\mathrm{i,j,k}-\phi_\mathrm{i,j,k-1}}{kT}\right)p_\mathrm{i,j,k-1}}{(z_\mathrm{k}-z_\mathrm{k-1})\frac{z_\mathrm{k+1}-z_\mathrm{k-1}}{2}} - \frac{R}{D_\mathrm{p}} = 0.\end{aligned} \tag{14}$$

3. *Boundaries and interfaces*

We assume Neumann boundary conditions for both the electrostatic potential and the charge densities. This means that at the borders of the calculation grid in normal direction the partial derivation of the electrostatic potential and the current densities for electrons and holes are zero. A precise derivation of the boundary conditions with respect to a minimization of the truncation error is given in Ref. [39] on page 172. Particular attention must be paid to the continuity condition for the electrostatic potential at the surface of the semiconductor. For a surface, which is nearly free of surface states, the normal component of the electric displacement field $\vec{D}$ remains constant at the transition from the semiconductor to the vacuum. With surface states being present within or even outside of the fundamental band gap, a surface charge distribution σ gives rise to a change of $\vec{D}$ according to Eq. (15),

$$\vec{n} \cdot (\vec{D}_\mathrm{vac} - \vec{D}_\mathrm{semi}) = \sigma, \tag{15}$$

where $\vec{n}$ is the normal vector of the surface. Using the relation for isotropic media $\vec{D} = -\epsilon_0\epsilon_\mathrm{r}\nabla\phi$ we obtain for a normal vector in the z direction

$$\epsilon_0\epsilon_\mathrm{r}\left.\frac{\partial\phi}{\partial z}\right|_\mathrm{semi} - \epsilon_0\left.\frac{\partial\phi}{\partial z}\right|_\mathrm{vac} - \sigma = 0. \tag{16}$$

Again, Eq. (16) can be discretized by employing difference operators [39]. Assuming that all points $z \geqslant z_\mathrm{surf}$ belong to the semiconductor, whereas all points $z < z_\mathrm{surf}$ belong to either the tip or the vacuum, Eq. (12) needs to be replaced for $z = z_\mathrm{surf}$

(or $k = k_{\text{surf}}$, respectively) by

$$\left(\frac{\frac{\phi_{\text{i+1,j,k}}-\phi_{\text{i,j,k}}}{x_{\text{i+1}}-x_{\text{i}}} - \frac{\phi_{\text{i,j,k}}-\phi_{\text{i-1,j,k}}}{x_{\text{i}}-x_{\text{i-1}}}}{\frac{x_{\text{i+1}}-x_{\text{i-1}}}{2}} + \frac{\frac{\phi_{\text{i,j+1,k}}-\phi_{\text{i,j,k}}}{y_{\text{j+1}}-y_{\text{j}}} - \frac{\phi_{\text{i,j,k}}-\phi_{\text{i,j-1,k}}}{y_{\text{j}}-y_{\text{j-1}}}}{\frac{y_{\text{j+1}}-y_{\text{j-1}}}{2}} \right.$$

$$\left. + \frac{\epsilon_{\text{r}}\epsilon_0 \frac{\phi_{\text{i,j,k+1}}-\phi_{\text{i,j,k}}}{z_{\text{k+1}}-z_{\text{k}}} - \epsilon_0 \frac{\phi_{\text{i,j,k}}-\phi_{\text{i,j,k-1}}}{z_{\text{k}}-z_{\text{k-1}}} + \sigma_{\text{i,j,k}}}{\frac{\epsilon_{\text{r}}\epsilon_0(z_{\text{k+1}}-z_{\text{k}})+\epsilon_0(z_{\text{k}}-z_{\text{k-1}})}{2}} \right)$$

$$- \frac{e}{\epsilon_0\epsilon_{\text{r}}} \frac{z_{\text{k}} - z_{\text{k-1}}}{\epsilon_{\text{r}}\,(z_{\text{k+1}} - z_{\text{k}}) + (z_{\text{k}} - z_{\text{k-1}})}$$

$$\times (n_{\text{i,j,k}} - p_{\text{i,j,k}} - N_{\text{D}}^{+} + N_{\text{A}}^{-}) = 0. \tag{17}$$

In the region of the semiconductor, Eqs. (12) (for $z > z_{\text{surf}}$), (17) (for $z = z_{\text{surf}}$), (13), and (14) have to be solved, whereas in the region of the vacuum only Eq. (12) has to be solved due to the absence of charge carriers. At the tip the electrostatic potential ϕ_{tip} is set to a constant value, the so-called contact potential $\Delta\phi$ [40]. It can be interpreted as the potential difference between the tip and the surface of the semiconductor,

$$\phi_{\text{tip}} = \Delta\phi = V + (E_{\text{F}} - E_{\text{C}} - \chi + \phi_{\text{m}})/e, \tag{18}$$

where V is the voltage applied between the tip and the semiconductor, χ is the electron affinity of the semiconductor, and ϕ_{m} is the work function of the tip.

4. *Initial values*

For the initial values of the electrostatic potential $\phi^0_{\text{i,j,k}}$ and the charge densities $n^0_{\text{i,j,k}}$ and $p^0_{\text{i,j,k}}$ within the semiconductor, one assumes that the tip is located infinitely far away from the semiconductor's surface. Hence, the semiconductor is initialized without tip-induced band bending and with equally distributed carrier concentrations:

$$\left.\begin{aligned} \phi^0_{\text{i,j,k}} &= 0\,\text{V} \\ n^0_{\text{i,j,k}} &= n_0 + c_{\text{light}} \\ p^0_{\text{i,j,k}} &= p_0 + c_{\text{light}} \end{aligned}\right\} \text{for } k \geqslant k_{\text{surf}}. \tag{19}$$

n_0 and p_0 (together with E_{F}) can be easily obtained by solving the charge neutrality condition $n_0 - p_0 - N_{\text{D}}^{+} + N_{\text{A}}^{-} = 0$, when the semiconductor is in equilibrium. The initial density of the light-excited carriers c_{light} can be estimated using

$$c_{\text{light}} = \alpha \frac{P_{\text{opt}}}{E_{\text{ph}} A_{\text{light}}} \tau, \tag{20}$$

where α is the absorption coefficient of the semiconductor, τ is the lifetime of the minority carriers, A_{light} is the illuminated surface area, P_{opt} is the optical power of the laser, and E_{ph} is the photon energy. One could also take into account that P_{opt} depends exponentially on the penetration depth of the photons. However, in p-type GaAs with $\alpha \sim 1 \times 10^4 \text{cm}^{-1}$ for $E_{\text{ph}} = 1.58$ eV [41], the change of P_{opt} in the region of interest is in the range of only a few percent and hence can be neglected.

For the given problem, one could have chosen other initial values that promise to converge faster to the optimal solution. For example, one could have estimated the tip-induced band bending within the semiconductor and used these values for $\phi^0_{\text{i,j,k}}$. However, in practice, the approach given by Eq. (19) delivers good results.

5. *Carrier generation and recombination*

The generation and recombination process is modeled by radiative band-to-band transitions. Since GaAs exhibits a direct band gap, this recombination process is taken to be dominant. The net recombination rate R_{te} in thermal equilibrium and without illumination is given by [42]

$$R_{\text{te}}(x,y,z) = b[n(x,y,z)p(x,y,z) - n_0 p_0], \tag{21}$$

where b is the bimolecular recombination coefficient. When the laser is switched on, electron-hole pairs will be created with a rate of $R_{\text{light}} = c_{\text{light}}/\tau$. In the absence of the tip-induced band bending (i.e., without a potential gradient for the carriers), a second equilibrium situation will be reached, when the net recombination rate equals R_{light}:

$$b[(n_0 + c_{\text{light}})(p_0 + c_{\text{light}}) - n_0 p_0] = R_{\text{light}}. \tag{22}$$

With the help of Eqs. (20) and (22), b can be determined and, finally, the net recombination rate R for the sample under illumination, suitable for the substituion in Eqs. (13) and (14), is given by

$$R(x,y,z) = b[n(x,y,z)p(x,y,z) - n_0 p_0] - R_{\text{light}}. \tag{23}$$

6. *Numerical iteration method*

The numerical iteration method used to solve Eqs. (12), (13), (14), and (17) should be discussed briefly. Although there exist many different approaches for the numerical solution of this system of nonlinear algebraic equations, we decided to use a successive over relaxation (SOR) Newton method because of the easy implementation and the advantage that Eqs. (12), (13), and (14) can be sequentially used to find the solution [39]. A derivation of this and other methods in detail is, for example, given by Selberherr [39]. Identifying Eqs. (12), (13), and (14) with $F_1(\phi,n,p) = 0$, $F_2(\phi,n,p) = 0$, and $F_3(\phi,n,p) = 0$, respectively, the variation of the variables $\delta\phi^{\text{k}} = \phi^{\text{k+1}} - \phi^{\text{k}}$, $\delta n^{\text{k}} = n^{\text{k+1}} - n^{\text{k}}$, and $\delta p^{\text{k}} = p^{\text{k+1}} - p^{\text{k}}$ of the kth iteration step of the SOR Newton method are evaluated by [39]

$$\begin{aligned} \delta\phi^{\text{k,m+1}} &= -\frac{\omega F_1(\phi^{\text{k}}, n^{\text{k}} + \delta n^{\text{k,m}}, p^{\text{k}} + \delta p^{\text{k,m}})}{\frac{\partial F_1^{\text{k}}}{\partial\phi}}, \\ \delta n^{\text{k,m+1}} &= -\frac{\omega F_2(\phi^{\text{k}} + \delta\phi^{\text{k,m+1}}, n^{\text{k}}, p^{\text{k}} + \delta p^{\text{k,m}})}{\frac{\partial F_2^{\text{k}}}{\partial n}}, \\ \delta p^{\text{k,m+1}} &= -\frac{\omega F_3(\phi^{\text{k}} + \delta\phi^{\text{k,m+1}}, n^{\text{k}} + \delta n^{\text{k,m+1}}, p^{\text{k}})}{\frac{\partial F_3^{\text{k}}}{\partial p}}, \end{aligned} \tag{24}$$

where ω is a relaxation parameter. This means that an "inner" iteration (index m) has to be performed for each Newton step k.

7. *Design of the mesh*

In order to obtain the potential near the surface with the required spatial accuracy, rather small distances between the points of the mesh used in the finite-difference calculation are needed (on the order of 0.1 nm). However, for lower doped semiconductors the band bending may extend deep

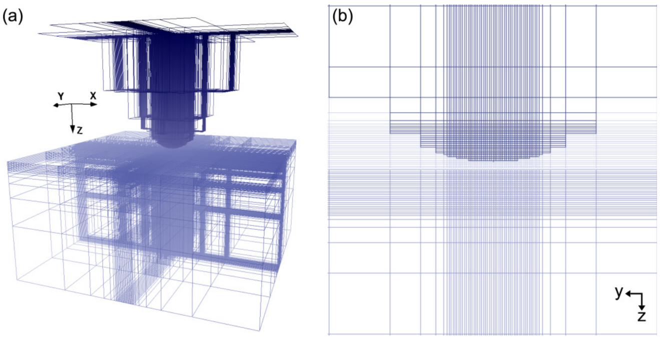

FIG. 2. (Color online) (a) Three-dimensional view of a mesh, similar to that used in our computations. The mesh points are located at the intersections of the lines. For the sake of clarity, the mesh consists only of one-eighth of the mesh points used in our computation. Additionally, the points in the vacuum are hidden. (b) Cross-sectional view of the central y-z plane (isometric projection) including the mesh points in the vacuum.

into the semiconductor (up to µm). Hence, the mesh needs to cover a volume large enough to include the full decay of the potential. In principle one could use a fully equidistant mesh, but the number of points needed would make the calculation impractical. At large distances (x, y, and z) from the semiconductor surface area facing the tip, the potential changes almost linearly and hence the points of the mesh can be increasingly separated in space. Along all three directions, we use equidistant points close to the surface area facing the tip. At larger distances we increase the point separation of the mesh, until the mesh volume is sufficiently large. Figure 2(a) illustrates a three-dimensional view of a mesh similar to that used in our computations. The mesh points are located at the intersections of the lines. For the sake of clarity, the mesh consists only of one-eighth of the mesh points used in our computation. Additionally, the points in the vacuum are hidden. Figure 2(b) represents a cross-sectional view along the central y-z plane (including mesh points in the vacuum). The truncation errors of the electrostatic potential and the carrier concentration due to the choice of the mesh are discussed in Ref. [39]. This mesh provides a full three-dimensional finite-difference calculation, where any tip shape can be modeled. It is not limited to hyperbolically shaped tips [22].

B. Calculation of the tunnel current

The calculation of the tunnel current density is based on the tunneling model developed in Refs. [21,43]. The current density is given by

$$J_{\mathrm{i}} = \frac{m_{\mathrm{e}} e}{2\pi^2 \hbar^3} \int_{E_{\mathrm{F}}+eV}^{E_{\mathrm{F}}} dE\, \Theta(\pm[E - E_{\mathrm{i}}]) \times \int_{E(1\mp m_{\mathrm{eff,i}})\pm m_{\mathrm{eff,i}} E_{\mathrm{i}}}^{E} dW\, D(W), \tag{25}$$

where $\Theta(E)$ is the step function. $D(W)$ is the energy (W)-dependent transmission coefficient in the WKB approximation given in Ref. [21]. It depends on the band-edge energies, obtained from the solution of the Poisson equation, along the axis perpendicular to the sample surface (z axis in the electrostatic calculation), through the tip apex.

This equation covers the tunneling of electrons out of the valence band ($i = \mathrm{V}$) and out of an electron accumulation zone in the conduction band ($i = \mathrm{C}$) into the empty tip states as well as of electrons in the tip into the empty conduction band states ($i = \mathrm{C}$) or into a hole accumulation zone in the valence band ($i = \mathrm{V}$). The total tunnel current I is the sum of all current density contributions J_{i} [see Eq. (25)] multiplied by the tunnel area A_{tunnel} [40]:

$$I = (J_{\mathrm{V}} + J_{\mathrm{C}}) \times A_{\mathrm{tunnel}}. \tag{26}$$

This approach assumes parabolic bands and does not incorporate the tunneling of light-excited carriers. Hence, the model is extended here in order to incorporate the concentrations of both minority and majority carriers (including light-excited carriers) obtained from the solution of the continuity equations. From these carrier concentrations we derive the quasi-Fermi levels $E_{\mathrm{FQ,C}}$ and $E_{\mathrm{FQ,V}}$, at the surface. $E_{\mathrm{FQ,C}}$ ($E_{\mathrm{FQ,V}}$) is the upper (lower) limit for the energy of the electrons (holes) in the conduction band (valence band) in the limit of $T = 0\,\mathrm{K}$. These electrons (holes) can tunnel from the conduction band (valence band) into the tip. Hence, the quasi-Fermi levels replace the upper limit of the first integral in Eq. (25).

The quasi-Fermi levels have to be determined precisely, because they affect critically the tunnel current density. Calculating the quasi-Fermi levels $E_{\mathrm{FQ,i}}$ on the basis of Eqs. (1) and (2) using the carrier densities $n(x,y,z)$ and $p(x,y,z)$ is only accurate enough for moderate carrier concentrations [$n\,(x,y,z) < N_{\mathrm{C}}$ and $p\,(x,y,z) < N_{\mathrm{V}}$], since the conduction band dispersion deviates from its parabolic approximation almost directly at E_{C}.

Hence, for higher carrier concentrations we need to integrate the calculated density of states [DOS(E)] of the investigated semiconductor (i.e., GaAs), e.g., taken from Chelikowsky and Cohen [44,45],

$$n' = \int_{E_{\mathrm{C}}}^{\infty} dE\, \mathrm{DOS}(E) f_{\mathrm{S}}(E - E_{\mathrm{FQ,C}}), \tag{27}$$

$$p' = \int_{-\infty}^{E_{\mathrm{V}}} dE\, \mathrm{DOS}(E) f_{\mathrm{S}}(E_{\mathrm{FQ,V}} - E), \tag{28}$$

and numerically solve these integrals for $E_{\mathrm{FQ,i}}$, such that n' (or p') equals the carrier concentration $n(x,y,z)$ [or $p(x,y,z)$] at the surface below the tip apex. The Fermi-Dirac distribution of the semiconductor $f_{\mathrm{S}}(E)$ is approximated by a step function here. The same approximation is already used in the derivation of the tunnel current [Eq. (25)] and hence does not restrict the validity further [43].

Additionally, the effective masses $m_{\mathrm{eff,i}}$ of the holes and electrons are taken to be energy-dependent. By substituting $E_{\mathrm{FQ,C}}$ ($E_{\mathrm{FQ,V}}$) and $n(x,y,z)$ [$p(x,y,z)$] into Eq. (1) [Eq. (2)], it can be solved for new quasieffective masses $m_{\mathrm{effq,C}}$ ($m_{\mathrm{effq,V}}$), replacing $m_{\mathrm{eff,C}}$ ($m_{\mathrm{eff,V}}$). The resulting quasieffective masses and quasi-Fermi levels are then used to calculate the tunnel current density.

V. RESULTS AND DISCUSSION

In this section, the measured spectra, as illustrated in Fig. 1, are analyzed and discussed. The quantitative description presented in Sec. IV is applied to compute the tunnel currents under different physical assumptions and parameters as well as with and without illumination. The results of the computation are fitted to the measured spectra, in order to test the validity of the quantitative description of photoexcited STS.

For the particular case of the GaAs(110) surface, a quantitative physical explanation of the measured tunnel spectra requires the inclusion of intrinsic surface states energetically located within the bands. The physical effect of the surface states on the illuminated tunneling spectra is described with two different models. For both models the tunnel currents are computed and fitted to the measured spectra, followed by a comparative discussion.

A. Effect of GaAs(110) surface states on the tunnel spectroscopy

At this stage we recall first the origin of the relevant tunnel current contributions followed by a discussion of the effect of surface states. Electrons can tunnel from the valence band into the tip, if the energy of the highest occupied state of the tip ($E_{\mathrm{F,tip}} = E_{\mathrm{F}} + eV$) is below the bulk valence band edge of the semiconductor. On the other hand, if $E_{\mathrm{F,tip}}$ is energetically above the bulk conduction band edge, tunneling of electrons from the tip into the conduction band is possible. These two processes usually form the main contributions of the tunnel current, denoted by I_{V} and I_{C}, respectively. In addition, an accumulation current I_{acc} can occur for n-type (p-type) semiconductors, if the conduction (valence) band is bent below (above) E_{F} near the surface (majority-carrier accumulation) [30]. For n-type surfaces the accumulation current arising from the electron accumulation zone in the conduction band I_{acc} was derived to be at least one order of magnitude larger than I_{V}. However, this was not confirmed by measurements on n-doped GaAs(110) surfaces [30]. Jäger *et al.* [30] and Ishida *et al.* [46] explained this discrepancy by the presence of surface states.

The GaAs(110) surface has two relevant intrinsic surface states located energetically within the bands. The filled one is close to the valence band edge and corresponds to the dangling bond above the As surface atoms. It is commonly labeled A_5 and has its energetic maximum at the Γ point of the surface Brillouin zone. The empty one is also a dangling bond state, but localized above the Ga surface atoms. It is energetically slightly above the conduction band edge with its minimum at the edge of the surface Brillouin zone ($\overline{X}$ point). It is commonly labeled C_3 [47–49]. All other surface states are deeper within the bands and hence not relevant here [47,50–52]. For the explanation of the discrepancy between measured and calculated accumulation current I_{acc}, only the empty C_3 surface state is important: Jäger *et al.* suggested that the accumulation current is suppressed, because the tip cannot accommodate conduction band electrons tunneling out of the empty C_3 surface state due to the nonzero parallel momentum [30]. Ishida *et al.* assumed in addition that the C_3 surface state can be partially filled, effectively pinning the Fermi level. This reduces the charge density in the accumulation layer and hence the magnitude of I_{acc} [46].

Measurements in this paper were performed on p-doped—not on n-type—GaAs(110) surfaces. The p-type GaAs(110) surface exhibits a Fermi level near the valence band edge. Without illumination, the minority-carrier concentration is too low to support an inversion layer (i.e., "accumulation" of electrons in the conduction band) near the surface under tunneling conditions [30]. Hence, in the dark no current could be supported from electrons tunneling out of the conduction band. The situation changes under illumination, when light-excited electrons are generated. These electrons behave like thermally excited electrons in the conduction band of an n-type sample. Thus, for p-type samples, a tunnel current similar to the accumulation current I_{acc} on an n-type sample arises from the tunneling of light-excited electrons out of the conduction band at negative sample voltages. This *photo-induced tunnel current* is denoted I_{photo} in the following (not to be confused with the current arising from the photoelectric effect).

In analogy to the explanations of the suppressed accumulation current on n-type GaAs(110) in the dark [30,46], we model the photoinduced tunnel current under two different physical conditions: full suppression of the accumulation current and hence the photoinduced tunnel current and a reduced electron accumulation due to surface-state-limited band bending.

B. Parameters of the calculation

For the calculations we assumed a hyperbolically shaped tip with a radius of curvature of 10 nm, an apex angle of 45°, and a work function of 4.5 eV. For the GaAs sample we used a p-type doping of 2×10^{18} cm^{-3}, an electron affinity of 4.07 eV, and bulk effective masses. The tip-sample separation was used as the only fitting parameter to adjust the calculated tunnel current to the measurement under dark conditions. The best fit was obtained for a tip-sample separation of 0.925 nm. The same value was used for all further calculations under illumination, since the spectra were measured at identical tip-sample separations. For the light-excited charge carriers we used a minority-carrier lifetime of 5×10^{-9} s for Zn-doped GaAs following Ref. [53] as well as hole and electron mobility values of 150 and 2400 cm^{2}V^{-1}s^{-1}, respectively [54]. The irradiance of the incident laser beam was used as the only fitting parameter for the calculation of the illuminated curves. The best fit values will be then compared with the experimentally used laser irradiance.

C. Results of the calculation

1. Full suppression of electron tunneling from the conduction band accumulation layer

We assume in this section that the light-excited carriers in the conduction band of our p-type GaAs(110) sample cannot tunnel into the tip ($I_{\mathrm{photo}} = 0$). The computational results are presented in Figs. 3–5. Figure 3 illustrates the band edge positions at the central axis through the tip as a function of the distance from the semiconductor surface for voltages of (a) −1.0 V and (b) +1.6 V without (dashed lines) and with (solid lines) illumination. Figures 4 and 5 show cross-sectional two-dimensional plots of (a) the electrostatic potential, (b) the electron concentration, and (c) the hole concentration through the central y-z plane for −1.5 V and

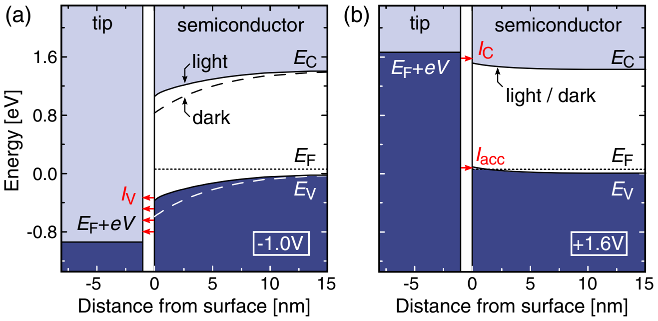

FIG. 3. (Color online) Calculated valence (E_V) and conduction (E_C) band-edge positions as a function of the distance from the semiconductor's surface for (a) negative (-1.0 V) and (b) positive (+1.6 V) voltages applied to the sample. The band-edge positions were calculated on the assumption that the surface states do not influence the band bending. The sample is shown on the right side at positive distance values. The Fermi energy (E_F) is close to the valence band edge in the bulk. The tip with its Fermi energy at $E_F + eV$ is shown on the left side. The dark blue (light blue) areas represent filled (empty) states. The band gap and the vacuum gap (tunnel barrier) between the surface (at 0 nm) and the tip position (at -0.925 nm) are shown in white. Dashed lines show the semiconductor's band edges without illumination, while solid lines correspond to the illuminated case. Note the reduced band bending under illumination.

+1.5 V, respectively, without (left frames) and with (central frames) illumination. The results correspond to the best fit of the model of full suppression of the photoinduced tunnel current to the experimental data, using an irradiance of the laser of $(22 \pm 5) \times 10^5$ Wm^{-2}. Note that the calculated tunnel current for the best-fitting solution will be shown and discussed in Sec. V D.

For negative voltages and under illumination, light-excited electrons accumulate near the surface [see Fig. 4(b2)]. The electron concentration near the surface locally reaches 6×10^{20} cm^{-3}. Note the color scale of the electron concentration in Fig. 4(b2) is reduced by a factor of 5×10^{-2} compared to the scale on the right side of Fig. 4(b3). This is 300 times larger than the hole concentration in the bulk. Under dark conditions [see Fig. 4(b1)], almost no free electrons are present and hence the density of electrons accumulating at the surface is almost zero, approximately a factor of 10^{16} smaller than under illumination. [Note the color scale of the electron concentration in Fig. 4(b1) is enhanced by a factor of 5×10^{14} to visualize the distribution.] In contrast, the hole concentration changes only slightly, when the laser is turned on [Figs. 4(c1) and 4(c2)]. The accumulated photoinduced electrons are screening the tip-induced band bending. The combined effect on the electrostatic potential ϕ is illustrated in Figs. 4(a1), 4(a2), and 3(a). For example, at an applied

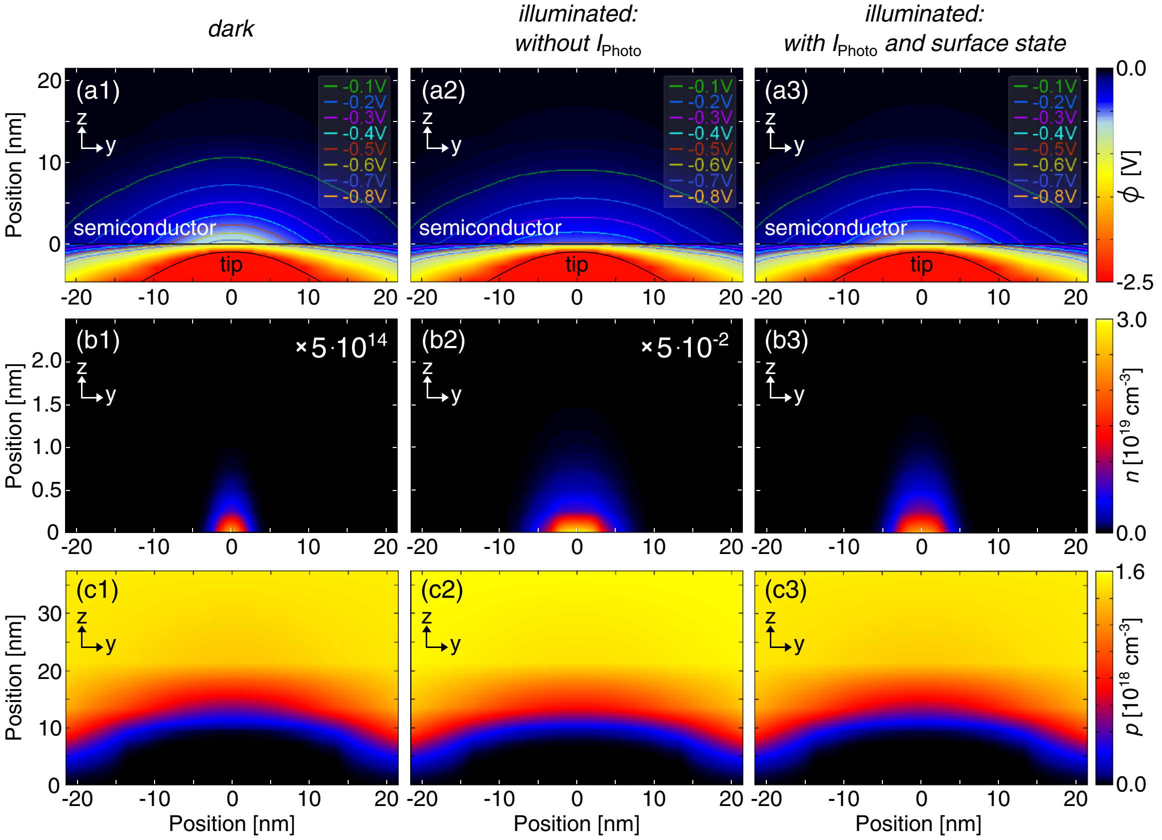

FIG. 4. (Color online) Cross-sectional plots of (a) the electrostatic potential ϕ of the tip-vacuum-semiconductor system, (b) the electron concentration n, and (c) the hole concentration p (in the semiconductor only) for a sample voltage of -1.5 V without illumination (left column), with illumination and no tunneling of photoinduced electrons in the surface accumulation layer $I_{\text{Photo}} = 0$ (central column), and with illumination, photoinduced tunnel current, and surface-state limited band bending (right column). The equipotential lines in (a) range from -0.1 V to -0.8 V in steps of 0.1 V.

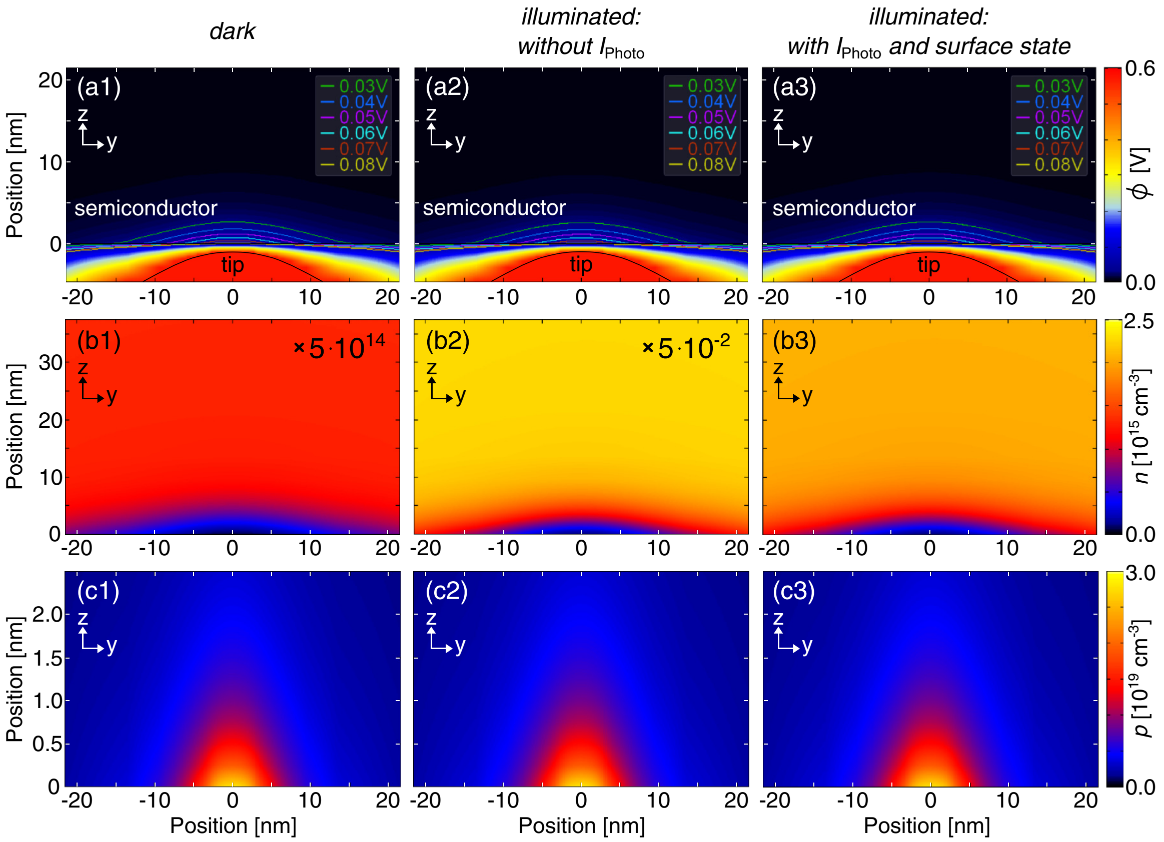

FIG. 5. (Color online) Cross-sectional plots of (a) the electrostatic potential ϕ of the tip-vacuum-semiconductor system, (b) the electron concentration n, and (c) the hole concentration p (in the semiconductor only) for a sample voltage of $+1.5$ V without illumination (left column), with illumination and no tunneling of photoinduced electrons in the surface accumulation layer $I_{\text{Photo}} = 0$ (central column), and with illumination, photoinduced tunnel current, and surface-state limited band bending (right column). The equipotential lines in (a) range from 0.03 to 0.08 V in steps of 0.01 V.

voltage of -1.0 V, ϕ decreases from -0.59 to -0.37 V when the sample is exposed to laser light. The reduced potential will, according to Eqs. (25) and (26), lead to an increased valence band tunnel current I_V in accordance with the experimental observation (Fig. 1).

For positive voltages, the screening is primarily determined by the thermally generated holes (accumulating at the surface) [Figs. 5(c1) and 5(c2)], since the concentration of light-excited holes is almost two orders of magnitude lower. The light-excited electrons move away from the surface [Figs. 5(b1) and 5(b2)]. Hence, the electron concentration near the surface is small, regardless of whether the laser is switched on or off. Thus, no significant change in the tip-induced band bending can be observed for the dark and illuminated cases in Figs. 3(b), 5(a1), and 5(a2). In consequence, no change in the tunnel current occurs at positive voltages in agreement with the experimental observation.

2. *Surface-state-limited band bending*

In this section, we assume that (i) the light-excited electrons can partially occupy the empty C_3 surface state, but a direct tunneling out of the surface state is negligible [20], and (ii) light-excited carriers can tunnel out of the conduction band ($|I_{\text{photo}}| > 0$). In analogy to Ref. [46] the C_3 surface state is modeled by a Gaussian distribution peaking at an energy E_{SS} of 0.33 eV above the conduction band minimum with a FWHM of 0.25 eV. We assume a surface state density of 4.4×10^{14} cm^{-2}, corresponding to one state per surface cation [46]. The surface state is electrically neutral, if it is positioned completely above the quasi-Fermi level of the conduction band ($E_{FQ,C}$). For positive voltages and thus upward band bending, the surface state will remain unoccupied and the band bending does not change. For negative voltages and downward band bending, the tail of the Gaussian distribution will move below the quasi-Fermi energy and thus create a negative surface charge distribution. This additionally screens the tip-induced band bending and hence reduces the bulk electron concentration near the surface. The resulting band-edge positions E_V and E_C are shown in Fig. 6 as a function of the distance from the surface. For comparison with the previously discussed model, the cross-sectional plots of the potential as well as electron and hole distributions are shown in the right columns of Figs. 4 and 5 for -1.5 and $+1.5$ V, respectively. Again, the screening arises from electrons filling the surface state and accumulating near the surface at negative voltages and from holes accumulating near the surface at positive voltages. The photoinduced tunnel current I_{photo} arises from photoexcited electrons in the conduction band, as indicated in Fig. 6(a).

Figure 7 shows the band edge positions E_V and E_C at the surface as a function of the applied voltage under illumination.

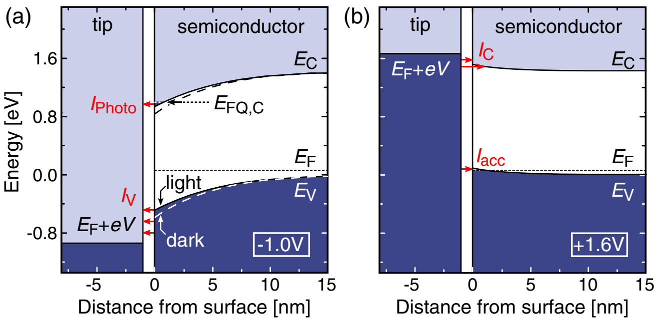

FIG. 6. (Color online) As described in the legend for Fig. 3, but calculated assuming that the empty surface state is partially filled and hence limits the tip-induced band bending. Shown are the band-edge positions under illumination (solid lines) and under dark conditions (dashed lines). I_{Photo} indicates the photo-induced tunnel current.

The quasi-Fermi levels $E_{\mathrm{FQ,V}}$ and $E_{\mathrm{FQ,C}}$ are drawn as dotted lines. The peak position of the Gaussian distribution of the C_3 state is drawn as a solid line and denoted E_{SS}. For the purpose of illustration an energy interval of 4σ around E_{SS} indicates the energetic width of the surface state. The occupied part of the distribution is marked as light pink area. Note that a partial occupation of the surface state is already sufficient to limit the tip-induced band bending.

Hence, in this model, the change of the tunnel current between the illuminated and dark case is caused by the limited band bending *and* the tunneling of light-excited electrons from the conduction band into the tip. The best fit of the surface state-limited band bending model to the experimental data is achieved using an irradiance of the laser of $(1^{+0.7}_{-0.3}) \times 10^5\ \mathrm{W\,m^{-2}}$.

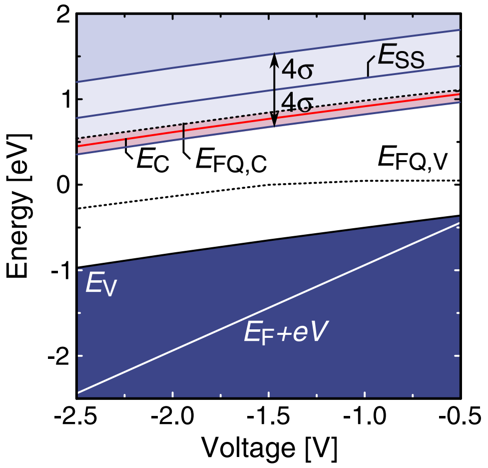

FIG. 7. (Color online) Band edge positions E_{V} and E_{C} at the surface as a function of the applied voltage under illumination. The quasi-Fermi levels $E_{\mathrm{FQ,V}}$ and $E_{\mathrm{FQ,C}}$ are drawn as dotted lines. The peak position of the Gaussian distribution is denoted E_{SS}, while an energy interval of 4σ around E_{SS} indicates the energetic extension of the surface state. The occupied part of the distribution is marked in light pink.

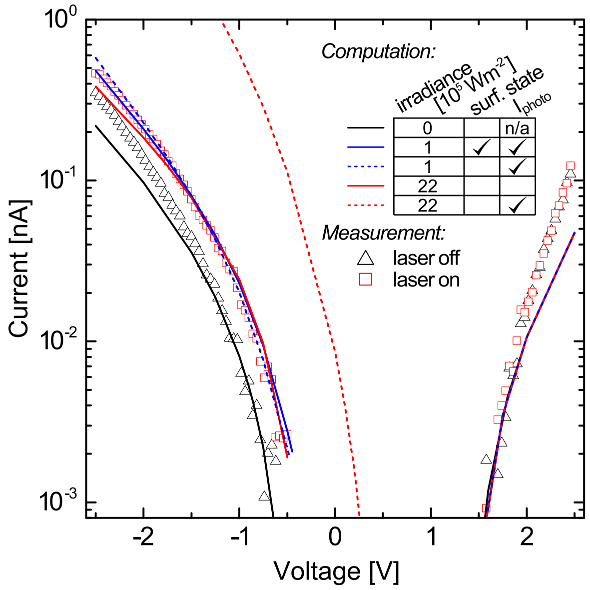

FIG. 8. (Color online) I-V curves obtained from a p-type GaAs sample with (red squares) and without (black triangles) illumination compared to computational results (solid and dashed lines). The fit of the current for dark conditions is represented by the black solid curve. The red solid line was calculated assuming full suppression of electron tunneling from the conduction band accumulation layer. The tunnel current at negative voltages arises from electrons tunneling out of the valence band only. The blue solid line shows the tunnel current for the case of the surface-state-limited band bending. Here the tunnel current is composed of a valence band current and a photoinduced tunnel current. The red dashed line was calculated using the same parameters as for the red solid curve, but assuming tunneling out of the photoexcited conduction band accumulation layer. Similarly, the blue dashed curve corresponds to a tunnel current, which was derived for the same parameters as for the blue solid curve, but assuming that the surface state cannot be electrically charged. The blue and red solid lines fit well to the experimental data, but require significantly different irradiance levels, given in the table (inset). Note, all the calculated spectra coincide at positive voltages and are shown as overlapping red-blue dashed line.

D. Comparison of the calculated and measured tunnel currents

Figure 8 shows the measured spectra under dark (black triangles) and illuminated (red squares) conditions taken from Fig. 1 together with the calculated currents (lines) under different conditions. First we concentrate on the spectra under dark conditions. The calculated current, which is shown as a black solid line, represents the best fit using only the tip-sample separation as a fitting parameter (0.925 nm). This tip-sample separation is a reasonable value for STM operation. Note that the calculated tunnel current under dark conditions is identical for both models. Good agreement is found between the onset voltages of the calculated black solid curve and of the experimental data (triangles).

At this stage, the criteria for the best fit need to be briefly discussed: The theoretical foundation of the tunnel current calculation is most accurate for the smallest voltages, i.e., at the onset voltages. In addition, the onset voltages of the tunnel current are also experimentally the most accurate features. Therefore, we chose those fits, which reproduce best the onset voltages and the initial current slope near the onset voltages. The deviation of the calculated curve from the measured data points at larger magnitudes of voltage is due to the nonparabolic bands at larger energies [55].

Under illumination, the tunnel current was fitted using the irradiance of the laser beam as the only fitting parameter. The tip-sample separation of 0.925 nm determined from the dark spectrum was kept constant, since the pair of dark and illuminated experimental spectra were measured at identical separations. The best fit of the calculated current, assuming full suppression of the photoinduced tunnel current, is shown as a solid red curve in Fig. 8. Note, the current at positive voltages is independent of the illumination and hence *all* the calculated curves coincide in this voltage range. The result matches the current and the onset voltages of the measured spectrum under illumination on the positive and negative branch.

In order to illustrate the magnitude of the photoinduced tunnel current, if not suppressed, the red dashed line was derived using the same laser irradiance as for the red solid curve, but assuming now that the photoinduced electrons can tunnel. The resulting total current is dominated by the photoinduced tunnel current and is more than one order of magnitude larger than the measured one. Note, the onset voltage for the negative branch is moved to a small positive voltage of 0.3 V. Electrons tunneling out of the sample already at positive voltages have been indeed experimentally observed previously for large laser irradiance [18,19].

The blue solid curve in Fig. 8 shows the best fit of the calculated current employing surface state-limited band bending including a photoinduced tunnel current (tunneling of light-excited electrons accumulated at the surface). It also agrees well with the measured spectrum, but the best fit is obtained for a significantly lower laser irradiance as compared to the red curve (see discussion below).

Finally, for illustration purposes only, we briefly discuss the case that the surface state cannot be occupied by electrons, although there is no experimental or theoretical evidence that the surface state cannot be charged when dragged below the Fermi energy at negative sample voltages. The absence of surface charges screening the electric field is in this case compensated by the accumulation of additional light-excited electrons at the surface. This leads to a slightly higher photoinduced tunnel current at large voltages, but similarly well fitting at small voltages (see blue dashed line in Fig. 8). The reduction of the current by surface state limited band bending is hence already detectable at the present small laser irradiance, but its effect should be much more pronounced at larger laser irradiances.

E. Comparison and discussion of the models

The solid blue and red lines in Fig. 8 demonstrate that both physically relevant models describe the slope, shape, and onset voltages of the measured spectrum under illumination on the positive and negative branch well. However, we can discriminate physically these different models on the basis of the laser irradiance: The best-fitting irradiance was found to be smaller for the surface-state-limited band-bending model [$(1^{+0.7}_{-0.3}) \times 10^5\ \mathrm{W m^{-2}}$] as compared to $(22 \pm 5) \times 10^5\ \mathrm{W m^{-2}}$ for the full suppression model of the photoinduced tunnel current.

The experimentally used laser irradiance (given in Sec. II) was $(1.45 \pm 0.44) \times 10^5\ \mathrm{W m^{-2}}$. This value agrees well only with the irradiance obtained using the surface-state-limited band-bending model including the photoinduced tunnel current. Experimentally, the laser irradiance required for the other model was not reached, and hence it can be discarded.

The comparison of the two models further demonstrates that the increased tunnel current due to laser illumination is not primarily due to an enhanced screening by photoinduced carriers. Instead the increased tunnel current arises primarily from direct tunneling of photoexcited minority carriers to the tip. An increased current solely due to enhanced screening without tunneling of photoexcited carriers would require much larger laser irradiances than the experimentally used one.

VI. CONCLUSIONS

A quantitative description of photoexcited scanning tunneling spectroscopy is developed and applied to experimental data measured on a p-doped GaAs(110) surface. The potential and charge-carrier distributions within the photoexcited tip-vacuum-semiconductor system is described by the Poisson as well as the hole and electron continuity equations, which are solved by a finite-difference algorithm. On the basis of the calculated potential and charge-carrier distributions, the different contributions to the tunnel current are calculated. Due to the presence of nonequilibrium charge carriers, the calculation of the tunnel current requires an extension of the tunnel current model of Feenstra and Stroscio, in order to include the quasi-Fermi levels of the light-excited carrier concentrations. For the GaAs(110) surface, the calculated tunnel currents for different physical models with and without illumination are fitted to the experimental data. The best fit is obtained for a tip-induced band bending, which is limited by the partial occupation of the empty C_3 surface state in the conduction band with light-excited electrons. The tunnel current at negative voltages is then composed of a valence band contribution and a photoinduced tunnel current of excited electrons in the conduction band. At positive voltages the tunneling of electrons into the conduction band dominates.

The quantitative description of the tunnel current under laser illumination developed here is generally applicable with few limitations only, which can, however, be easily accommodated. For example, semiconductors with complex band structures (e.g., indirect band gap) may require a more general form of the tunnel current [Eq. (25)] and in case of low carrier mobilities different carrier recombination processes may have to be considered [Eq. (23)]. Similarly, for the surface state a more elaborate model may be needed if the physical relevant part of its dispersion is not at the minimum (or maximum) (e.g., as for half-filled midgap surface states).

How can the quantitative description developed here be applied to other materials? Excited charge carriers are particularly relevant in solar cell structures and in light-emitting devices, where the spatial distribution of charge carriers, e.g., at defects and interfaces, is critically affecting the efficiency. In order to measure local charge-carrier distributions quantitatively with (preferably) atomic resolution by STM, one needs to correlate the tunnel current with the excited charge-carrier concentrations. The quantitative description developed here closes this gap, by putting the interpretation of photoexcited (as well as nonexcited) tunneling spectra of many different systems on a solid quantitative foundation. By fitting the calculated tunnel current to tunneling spectra with light-excited carriers using as reference spectrum the simultaneously measured dark spectrum, we obtain the best fit value of the laser irradiance, which is directly connected to the charge-carrier concentration. Thereby, we can extract from the pairs of dark and illuminated tunneling spectra the locally present excited charge-carrier concentration. By doing this spatially resolved one may ultimately derive maps of the local excited charge-carrier concentration. Hence, the quantitative description developed here promises to reach significantly deeper physical insight in the physical processes and behavior of excited charge carriers in semiconducting materials.

ACKNOWLEDGMENTS

The authors thank K. H. Graf for technical support, H. Eisele, R. M. Feenstra, and S. Selberherr for scientific discussions, as well as the Impuls- und Vernetzungsfonds of the Helmholtz-Gemeinschaft Deutscher Forschungszentren under Grant No. HIRG-0014 and the Deutsche Forschungsgemeinschaft under Grant No. Eb 197/5-1 for financial support.

---

[1] R. J. Hamers and K. Markert, Phys. Rev. Lett. **64**, 1051 (1990).
[2] Y. Kuk, R. S. Becker, P. J. Silverman, and G. P. Kochanski, Phys. Rev. Lett. **65**, 456 (1990).
[3] For the photoexcited scanning tunneling microscopy and spectroscopy, different but essentially synonymous terms are used in the literature, such as laser or light-excited, photo- or laser-assisted, light-modulated, optically pumped, and laser-combined STM, STM under (laser) irradiation, photoinduced tunnel current, or photovoltage imaging (using STM).
[4] T. W. Matthes, C. Sommerhalter, A. Rettenberger, M. Böhmisch, J. Boneberg, M. C. Lux-Steiner, and P. Leiderer, Applied Surf. Sci. **123/124**, 187 (1998).
[5] S. Aloni, I. Nevo, and G. Haase, Phys. Rev. B **60**, R2165 (1999).
[6] S. Aloni, I. Nevo, and G. Haase, J. Chem. Phys. **115**, 1875 (2001).
[7] S. Yoshida, Y. Kanitani, R. Oshima, Y. Okada, O. Takeuchi, and H. Shigekawa, Phys. Rev. Lett. **98**, 026802 (2007).
[8] S. Yoshida, Y. Kanitani, O. Takeuchi, and H. Shigekawa, Appl. Phys. Lett. **92**, 102105 (2008).
[9] S. Yoshida, Y. Kanitani, R. Oshima, Y. Okada, O. Takeuchi, and H. Shigekawa, Jpn. J. Appl. Phys. **47**, 6117 (2008).
[10] S. Landrock, Y. Jiang, K. H. Wu, E. G. Wang, K. Urban, and Ph. Ebert, Appl. Phys. Lett. **95**, 072107 (2009).
[11] S. Grafström, J. Appl. Phys. **91**, 1717 (2002).
[12] M. McEllistrem, G. Haase, D. Chen, and R. J. Hamers, Phys. Rev. Lett. **70**, 2471 (1993).
[13] T. Takahashi and M. Yoshita, Appl. Phys. Lett. **68**, 3479 (1996).
[14] T. Takahashi and M. Yoshita, Appl. Phys. Lett. **70**, 2162 (1997).
[15] N. D. Jäger, Ph. Ebert, K. Urban, R. Krause-Rehberg, and E. R. Weber, Phys. Rev. B **65**, 195318 (2002).
[16] K. Arima, H. Kakiuchi, M. Ikeda, K. Endo, M. Morita, and Y. Mori, Jpn. J. Appl. Phys. **43**, 1891 (2004).
[17] S. Yoshida, J. Kikuchi, Y. Kanitani, O. Takeuchi, H. Oigawa, and H. Shigekawa, e-J. Surf. Sci. Nanotechnol. **4**, 192 (2006).
[18] M. W. J. Prins, R. Jansen, R. H. M. Groeneveld, A. P. van Gelder, and H. van Kempen, Phys. Rev. B **53**, 8090 (1996).
[19] C. Sommerhalter, T. W. Matthes, J. Boneberg, P. Leiderer, and M. C. Lux-Steiner, J. Vac. Sci. Technol. B **15** (1997).
[20] D. Vu, S. Arscott, E. Peytavit, R. Ramdani, E. Gil, Y. André, S. Bansropun, B. Gérard, A. C. H. Rowe, and D. Paget, Phys. Rev. B **82**, 115331 (2010).
[21] R. M. Feenstra and J. A. Stroscio, J. Vac. Sci. Technol. B **5**, 923 (1987).
[22] R. M. Feenstra, J. Vac. Sci. Technol. B **21**, 2080 (2003).
[23] Ph. Ebert, M. Heinrich, M. Simon, K. Urban, and M. G. Lagally, Phys. Rev. B **51**, 9696 (1995).
[24] U. Semmler, M. Simon, Ph. Ebert, and K. Urban, J. Chem. Phys. **114**, 445 (2001).
[25] U. Semmler, M. Simon, Ph. Ebert, and K. Urban, J. Chem. Phys. **115**, 7330 (2001).
[26] Ph. Ebert, K. Urban, L. Aballe, C. H. Chen, K. Horn, G. Schwarz, J. Neugebauer, and M. Scheffler, Phys. Rev. Lett. **84**, 5816 (2000).
[27] Ph. Ebert and K. Szot, in *Nanoelectronics and Information Technology*, edited by R. Waser (Wiley-VCH, Weinheim, 2012), 3rd ed., Chap. 11, pp. 255–281.
[28] D. Mehtani, N. Lee, R. D. Hartschuh, A. Kisliuk, M. D. Foster, A. P. Sokolov, F. Čajko, and I. Tsukerman, J. Optics A **8**, S183 (2006).
[29] V. Tsukruk and S. Singamaneni, *Scanning Probe Microscopy of Soft Matter: Fundamentals and Practices* (Wiley-VCH, Weinheim, 2012).
[30] N. D. Jäger, E. R. Weber, K. Urban, and Ph. Ebert, Phys. Rev. B **67**, 165327 (2003).
[31] R. Maboudian, K. Pond, V. Bressler-Hill, M. Wassermeier, P. Petroff, G. Briggs, and W. Weinberg, Surf. Sci. **275**, L662 (1992).
[32] R. Dombrowski, C. Steinebach, C. Wittneven, M. Morgenstern, and R. Wiesendanger, Phys. Rev. B **59**, 8043 (1999).
[33] M. Wenderoth, M. A. Rosentreter, K. J. Engel, A. J. Heinrich, M. A. Schneider, and R. G. Ulbrich, Europhys. Lett. **45**, 579 (1999).
[34] Ph. Ebert, L. Ivanova, and H. Eisele, Phys. Rev. B **80**, 085316 (2009).
[35] N. D. Jäger, K. Urban, E. R. Weber, and Ph. Ebert, Appl. Phys. Lett. **82**, 2700 (2003).
[36] P. H. Weidlich, R. E. Dunin-Borkowski, and Ph. Ebert, Phys. Rev. B **84**, 085210 (2011).
[37] R. Seiwatz and M. Green, J. Appl. Phys. **29**, 1034 (1958).
[38] S. M. Sze and K. K. Ng, *Physics of Semiconductor Devices*, 3rd ed. (Wiley-Interscience, New York, 2007).
[39] S. Selberherr, *Analysis and Simulation of Semiconductor Devices* (Springer, Vienna/New York, 1984).
[40] R. M. Feenstra, Y. Dong, M. P. Semtsiv, and W. T. Masselink, Nanotechnol. **18**, 044015 (2007).

[41] H. C. Casey, D. D. Sell, and K. W. Wecht, J. Appl. Phys. **46**, 250 (1975).

[42] R. A. Smith, *Semiconductors* (Cambridge University Press, Cambridge, 1959).

[43] J. Bono and R. H. Good, Surf. Sci. **175**, 415 (1986).

[44] J. R. Chelikowsky and M. L. Cohen, Phys. Rev. B **14**, 556 (1976).

[45] J. R. Chelikowsky and M. L. Cohen, Phys. Rev. B **30**, 4828 (1984).

[46] N. Ishida, K. Sueoka, and R. M. Feenstra, Phys. Rev. B **80**, 075320 (2009).

[47] J. Chelikowsky and M. Cohen, Solid State Commun. **29**, 267 (1979).

[48] J. Chelikowsky and M. Cohen, Solid State Commun. **30**, 819 (1979).

[49] H. Carstensen, R. Claessen, R. Manzke, and M. Skibowski, Phys. Rev. B **41**, 9880 (1990).

[50] Ph. Ebert, B. Engels, P. Richard, K. Schroeder, S. Blügel, C. Domke, M. Heinrich, and K. Urban, Phys. Rev. Lett. **77**, 2997 (1996).

[51] B. Engels, P. Richard, K. Schroeder, S. Blügel, Ph. Ebert, and K. Urban, Phys. Rev. B **58**, 7799 (1998).

[52] Ph. Ebert, Curr. Opinion Sol. State Mat. Sci. **5**, 211 (2001).

[53] C. M. Colomb, S. A. Stockman, N. F. Gardner, A. P. Curtis, G. E. Stillman, T. S. Low, D. E. Mars, and D. B. Davito, J. Appl. Phys. **73**, 7471 (1993).

[54] U. Rössler and D. Strauch, eds., *Semiconductors, Group IV Elements, IV-IV and III-V Compounds. Part b - Electronic, Transport, Optical and Other Properties*, Landolt-Börnstein, New Series, Vol. III/41a1b (Springer, Berlin, 2001).

[55] M. Schnedler, Y. Jiang, K.H.Wu, E. Wang, R. Dunin-Borkowski, and Ph. Ebert, Surf. Sci. **630**, 225 (2014).